Nanoscale

PAPER

View Article Online
View Journal | View Issue

Cite this: *Nanoscale*, 2025, **17**, 18173

Influence of excitation pulse duration on the efficiency of upconversion nanoparticle-based FRET†

Alejandro Casillas-Rubio, [a] Khouloud Hamraoui,[b] Diego Mendez-Gonzalez, [b] Marco Laurenti, [b] Jorge Rubio-Retama,[b] Oscar G. Calderón *[a] and Sonia Melle *[a]

Received 30th April 2025,
Accepted 16th July 2025

DOI: 10.1039/d5nr01779c

rsc.li/nanoscale

Accurate and reliable quantification of Förster Resonance Energy Transfer (FRET) is essential for the development of sensitive upconverting nanoparticle (UCNP)-based biosensors. While lifetime-based FRET measurements are generally considered robust, excitation conditions can significantly bias observed efficiencies. Here, we investigate how excitation pulse width and power influence lifetime-derived FRET efficiency in core–shell β-$NaYF_4$:$Yb_{0.2}$@$NaYF_4$:$Yb_{0.2}$,$Er_{0.02}$ UCNPs functionalized with Cy3 dyes. Time-resolved upconversion luminescence (UCL) measurements reveal that apparent FRET efficiencies decrease with increasing excitation pulse duration and power. These variations stem from excitation-induced changes in the UCL lifetime, arising from the complex dynamics that accompany the upconversion emission process. A dynamic rate equation model reproduces the experimental trends, confirming that excitation parameters alter emissive state kinetics and thus bias lifetime-based FRET measurements. Our findings identify excitation conditions as a hidden variable in UCNP-FRET experiments and underscore the need for standardized measurement protocols.

1 Introduction

Förster Resonance Energy Transfer (FRET) is a non-radiative energy transfer mechanism that occurs between a donor and an acceptor fluorophore through long-range dipole–dipole interactions.[1–5] The efficiency of this process is governed by several critical parameters such as, the extent of spectral overlap between the donor's emission and the acceptor's absorption spectra, the intermolecular distance (typically within 1–10 nm), and the relative orientation of the donor and acceptor transition dipole moments. FRET efficiency inversely correlates with the sixth power of the donor–acceptor distance, making it a highly sensitive molecular ruler for probing nanoscale interactions and conformational dynamics in biological and material systems[6,7] Traditionally, FRET is evaluated by monitoring changes in the luminescence intensity of the donor and/or acceptor.[8] Classical fluorophores, such as organic dyes and quantum dots, have been widely used in FRET studies, enabling sensitivities down to the single-pair level. However, intensity-based methods are often prone to artifacts arising from various factors, including small Stokes shifts, broad emission spectra, crosstalk in multicomponent systems, photobleaching, reabsorption, scattering, and concentration-dependent effects. These issues can distort the actual FRET signal and introduce significant bias in data interpretation.[9]

To circumvent these potential limitations and enhance the reliability of FRET measurements, time-resolved luminescence measurements are frequently employed. In this approach, a reduction in the donor's excited-state lifetime, resulting from the introduction of an additional non-radiative relaxation pathway, serves as a direct and unambiguous indicator of FRET. This makes lifetime-based FRET measurements a powerful tool for quantifying nanoscale interactions in complex environments.

In this context, upconversion nanoparticles (UCNPs) have emerged as highly promising FRET donors due to their unique photophysical properties. These nanomaterials can efficiently convert near-infrared (NIR) light into visible emission through a nonlinear anti-Stokes process, resulting in background-free luminescence, which minimizes interference from autofluores-

[a]*Department of Optics, Complutense University of Madrid, E-28037 Madrid, Spain. E-mail: oscargc@ucm.es, smelle@fis.ucm.es*
[b]*Department of Chemistry in Pharmaceutical Sciences, Complutense University of Madrid, E-28040 Madrid, Spain*

†Electronic supplementary information (ESI) available: *Z*-Potential of UCNPs-PAA and UCNPs-PAA-PEI; dynamic light scattering of UCNPs-PAA; experimental UCL lifetime measurements system; fitting procedure for UCL decay curves; measurement of laser beam diameter; experimental conditions for the lifetime experiments; evaluation of the spectral overlap integral; full temporal evolution of UCL emission; temporal profile of Cy3 emission; parameter values used in the theoretical model. See DOI: https://doi.org/10.1039/d5nr01779c

cence and enhances the signal-to-noise ratio in complex biological media.[10,11] In addition, their exceptional photostability, resistance to photobleaching, narrow emission bands, long luminescence lifetimes (μs–ms range) and tunable emission spectra make them ideal candidates for donor pairs in FRET-based applications. Current research efforts focus on improving FRET efficiency by optimizing key parameters such as, UCNP-acceptor distance,[12,13] surface coatings,[14] and by reducing the presence of surface quenching processes.[15,16] In this vein, recent advances in UCNP synthesis have enabled the preparation of highly monodisperse nanoparticles with well-controlled size, crystal phase, and surface chemistry, thereby facilitating their integration into FRET-based systems.[17–25]

Recent studies have shown that the upconversion luminescence (UCL) lifetime, often used to quantify FRET efficiency, exhibits a more complex behavior than previously assumed. While the luminescence decay time has traditionally been attributed solely to the intrinsic lifetime of the emitting state, it is now understood that the UCL lifetime reflects the temporal dynamics of the entire upconversion process. This includes not only radiative transitions, but also energy transfer between sensitizers and activators, cross-relaxation processes, and the kinetics of intermediate excited states.[26] Thus, for instance, Chai *et al.*[27] demonstrated that the green UCL lifetime in Yb^{3+}–Er^{3+} codoped UCNPs is significantly shortened when the excited state of the Yb^{3+} sensitizer is quenched by fluorophores attached to the nanoparticle surface. Similarly, Bergstrand *et al.*[28] showed that in Yb^{3+}–Er^{3+} nanorods the UCL lifetime only approaches the intrinsic lifetime of the emitting Er^{3+} state when the Yb^{3+} excited state exhibits a much shorter lifetime and cross-relaxation processes involving the emitting level are negligible. Altogether, these findings underscore that the upconversion luminescence (UCL) lifetime is strongly influenced by the migration of excitation energy stored in the long-lived excited states of the sensitizer network, and is therefore highly dependent on excitation conditions such as pump power and pulse duration.[29]

Indeed, power-dependent variations in UCL lifetime have been widely reported, revealing complex dependencies on multiple experimental and material parameters.[30–32] These include nanoparticles size and architecture (*e.g.*, core *vs.* core–shell), excitation irradiance range, dopant composition, and the physical form of the sample (powder *vs.* solution). For instance, Han *et al.*[33] observed that the UCL lifetime of $NaLuF_4$:Yb,Er microrods in powder increased with excitation power (from 3 to 25 W cm^{-2}) when using pulses up to 1 ms. In contrast, single-particle studies using $NaYF_4$:$Yb_{0.2}$,$Er_{0.02}$@$NaYF_4$ core–shell UCNPs revealed a decrease in UCL lifetime with increasing excitation power for particles larger than 30 nm, with saturation observed at 10^5–10^7 W cm^{-2}.[30] Notably, smaller particles exhibited negligible lifetime variation under the same conditions. For example, Teitelboim *et al.*[32] reported that the UCL lifetime of core–shell UCNPs remained relatively insensitive to excitation power when using 4 ms pulses, unless the Er^{3+} doping concentration was increased, in which case higher power led to lifetime shortening. This power dependence was attributed to the initial distribution of excited-state populations at the onset of the decay, which is governed by the excitation conditions and, in turn, determines the population dynamics and the resulting luminescence decay.

Excitation pulse width has also been shown to significantly influence UCL dynamics. Han *et al.*[31] demonstrated a substantial 20-fold change in the 540 nm emission lifetime of Er^{3+} in $NaLuF_4$:$Yb_{0.9}$,$Er_{0.02}$ microrods by varying the excitation pulse width. More recently, Gao *et al.*[34] reported a pulse-width-dependent increase of up to 68% in the green emission lifetime for 20 nm $NaYF_4$:$Yb_{0.05}$,$Er_{0.02}$ nanoparticles. Their study further revealed that surface passivation plays a critical role: nanoparticles coated with an inert $NaYF_4$ shell showed a much smaller lifetime variation (12%) compared to ligand-free nanoparticles (267%). They also found that nanoparticles with higher Yb^{3+} concentration and lower Er^{3+} content were less sensitive to pulse variations. In a previous work[35] we reported a significant variation in UCL lifetime with the excitation pulse width, laser power, and excitation area concluding that laser fluence is the key parameter governing UCL decay dynamics, as it dictates the population distribution of energy levels at the moment the excitation pulse ends. This behavior was consistently observed across UCNPs with different sizes, surface coatings, solvents, host matrices, and Yb^{3+}/Er^{3+} doping ratios.

These excitation-dependent variations in UCL lifetime have important implications for the sensitivity and accuracy of FRET-based assays employing UCNPs as donors. Some studies have recently reported discrepancies between FRET efficiencies obtained from steady-state intensity measurements and those derived from lifetime-based approaches.[14,35–37] Notably, Kotulska *et al.*[37] reported that the excitation pulse duration plays a critical role in determining FRET sensitivity. In their work, short excitation pulses (10 ns) provided significantly higher FRET efficiency compared to long pulses (4 ms) in a $NaYF_4$:$Yb_{0.2}$,$Er_{0.02}$-Rose Bengal donor–acceptor system. Similarly, Bhuckory *et al.*[38] argued that UCL lifetime may not be a reliable parameter for assessing FRET efficiency, due to its complex dependence on excitation conditions and the underlying upconversion dynamics.

In this work, we aim to systematically investigate the influence of excitation pulse duration and power on FRET efficiency in UCNP-based systems by combining time-resolved upconversion luminescence measurements with theoretical modeling. To this end, core–shell $NaYF_4$:Yb^{3+}@$NaYF_4$:Yb^{3+},Er^{3+} nanoparticles with two different active shell thicknesses were synthesized and covalently functionalized with Cy3 acceptor dyes. By tuning the excitation pulse duration over several orders of magnitude and carefully controlling the excitation power, we demonstrate that the FRET efficiency determined from luminescence lifetime analysis is strongly dependent on excitation conditions. Our results reveal that short excitation pulses yield higher apparent FRET efficiencies, while long pulses result in significant underestimation. These experimental findings are supported by a comprehensive rate equation model that captures the dynamic interplay between donor excitation, radiative and non-radiative relaxation processes, and donor–acceptor energy transfer.

2 Experimental section

2.1 Chemicals

Yttrium(III) chloride hexahydrate ($YCl_3{\cdot}6H_2O$, 99.99%), ytterbium(III) chloride hexahydrate ($YbCl_3{\cdot}6H_2O$, 99.9%), erbium(III) chloride hexahydrate ($ErCl_3{\cdot}6H_2O$, 99.9%), 1-octadecene (ODE, 90%), oleic acid (OA, 90%), sodium hydroxide (98%), ammonium fluoride (98%), methanol (99.9%), dimethyl sulfoxide (DMSO, 99.9%), *N*,*N*-dimethylformamide (DMF, 99%), nitrosyl tetrafluoroborate ($NOBF_4$, 95%), ethanol absolute (EtOH), *n*-hexane (97%), acetone (99%), sodium trifluoroacetate (NaTFA) (98%), trifluoroacetic acid (TFA) (99%), polyethylenimine branched average MW approx. 800 by LS (PEI), *N*,*N*-diisopropylethylamine (DIPEA) (99%), *N*-(3-(dimethylamino) propyl)-*N*′-ethylcarbodiimide hydrochloride (99%), and *N*-hydroxysulfosuccinimide sodium salt (sulfo-NHS) (98%), were purchased from Sigma-Aldrich (Merck). Ethanolamine (99%) was purchased from Fluka Analytical, poly(acrylic acid) (PAA), 50 wt% solution in water; approx. MW 3000 to 5000 was purchased from Thermo Fisher Scientific. Sulfo-Cyanine3 NHS ester was purchased from Lumiprobe.

2.2 Synthesis of β-$NaYF_4$:Yb^{3+} core nanoparticles

The synthesis of β-$NaYF_4$:$Yb_{0.2}$ core sample was carried out by the thermal co-precipitation method as reported by Mendez-Gonzalez *et al.*[39] with slight modifications. First, $YCl_3{\cdot}6H_2O$ (0.40 mmol), and $YbCl_3{\cdot}6H_2O$ (0.10 mmol) were dissolved in 1 mL of MeOH. Then, this solution was poured into a three-necked round-bottom flask, which contained a binary solvent mixture of oleic acid (OA; 6 mL) and 1-octadecene (ODE; 15 mL). The mixture was heated at 140 °C in a nitrogen atmosphere under stirring. In order to eliminate any remaining traces of water, methanol, and hydrochloric acid, the temperature was then kept constant for 20 minutes while the flask was attached to a vacuum pump. After that, the mixture was degassed and then cooled to room temperature, and 74 mg of NH_4F (2 mmol) and 50 mg of NaOH (1.25 mmol) per 0.5 mmol of rare earth (RE) chlorides dissolved in 10 mL methanol were added simultaneously. The resultant solution was stirred at 25 °C for 30 min. Then, the mixture was heated up to 110 °C under an N_2 atmosphere and kept for 20 min under vacuum to remove methanol traces. The temperature was then increased to 315 °C, and the solution was kept for 1 h under N_2 atmosphere. Later, the solution was cooled down to room temperature, the crude UCNPs synthesis was mixed methanol, shaken, and allowed the phases to separate. The methanol phase was removed, this process was repeated twice, and then the UCNPs were precipitated *via* centrifugation at 8500 rpm for 20 min. Next, the product was washed twice with absolute ethanol, by centrifugation at 8500 rpm for 20 min. Finally, the purified oleate capped UCNPs were dispersed in 5 mL of hexane, and stored for further experiments.

2.3 Synthesis of core–shell $NaYF_4$:Yb^{3+},Er^{3+} UCNPs

Firstly, a stock rare earth (RE) precursor solution was prepared in order to grow an active-shell around β-$NaYF_4$:Yb^{3+} core nanoparticles. The protocol was as follows: 2 mmol of rare earth chlorides [78% of $YCl_3{\cdot}6H_2O$, 20% of $YbCl_3{\cdot}6H_2O$, and 2% of $ErCl_3{\cdot}6H_2O$] were dissolved in 10 mL of TFA at 90 °C in a three-neck flask. The evaporation of the mixture under a continuous flow of N_2 yields $Y(TFA)_3$, $Yb(TFA)_3$ and $Er(TFA)_3$ as a white solid powder. After preparing the 2 mmol rare earth $(TFA)_3$ precursors, they were dissolved in 6.4 mL of OA with 2 mmol NaTFA, heated at 150 °C for 30 minutes under N_2 atmosphere and then for 10 additional minutes under vacuum in order to remove traces of by-products. Later, the solution was cooled down to room temperature. The resulting transparent, yellow-colored stock RE solution was stored for the subsequent injection process.

Core–shell UCNPs with different $NaYF_4$:$Yb_{0.2}$,$Er_{0.02}$ shell thicknesses were prepared following a seed-mediated epitaxial growth procedure using the as-prepared β-$NaYF_4$:$Yb_{0.2}$ UCNPs as the cores (see section 2.2). In brief, a mixture of β-$NaYF_4$:$Yb_{0.2}$ (2.5 mL, hexane dispersion with a NP concentration of ≃12 mg mL^{-1}), 7 mL OA, and 7 mL ODE were first heated to 110 °C and kept at this temperature for 30 min under N_2 flow to remove hexane traces. Then we increased the temperature up to 310 °C at a heating rate of 5 °C per minute and kept it at 310 °C for 1 h under N_2 gas protection. During this temperature increase to 310 °C we added a total of 1.6 mL of the RE precursor solution prepared before, by splitting the 1.6 mL into 8 different (0.2 mL) injections. The first injection started when the temperature reached 180 °C, and the remaining injections where added with a 15 min interval between each other. The resultant core@shell UCNPs with a core to shell 0.25/0.5 RE molar ratio were precipitated, redispersed in 1 mL hexane, washed with ethanol by centrifugation (8500 rpm for 20 min) and finally dispersed in 5 mL hexane.

The procedure for the preparation of core–shell UCNPs with a core to shell 0.25/1 RE molar ratio is similar to the one for core@shell UCNPs with a 0.25/0.5 ratio, starting with the same concentration of β-$NaYF_4$:$Yb_{0.2}$ core nanoparticles. For the seed-mediated shell growth, 3.2 mL of stock precursor solution was used in this case. The samples were named CS1, CS2 for molar ratio 0.25/0.5, and 0.25/1, respectively, relative to the total amount in the core synthesis step to the shell growth step.

2.4 Water-soluble PAA encapsulated core–shell UCNPs

First, 2 ml of β-$NaYF_4$:$Yb_{0.2}$@$NaYF_4$:$Yb_{0.2}$,$Er_{0.02}$ (*ca.* 8 mg mL^{-1}) UCNPs dispersed in hexane were added to 5 ml *N*,*N*-dimethylformamide (DMF) solution that contains 140 mg of nitrosonium tetrafluoroborate ($NOBF_4$) and kept under vigorous stirring at room temperature. The reaction was let to proceed until transfer of UCNPs from the hexane phase to the DMF phase was observed (typically after 10 min). Subsequently, 5 ml toluene and 5 ml hexane were added, and the mixture was centrifuged at 11 000 rpm for 30 minutes. This process was repeated twice.

The precipitate was collected and dispersed in 5 ml DMF. Next, 500 mg poly(acrylic acid) (PAA) was added to the DMF solution, which was then heated to 80 °C for 1 h with vigorous stirring. Thereafter, the resultant PAA-coated UCNPs were puri-

fied by adding 5 mL of acetone and centrifuging at 11 000 rpm for 20 minutes, then redispersing and washing twice with Milli-Q water (1 mL in each Eppendorf tube) by centrifuging at 11 000 rpm for 20 minutes. Finally, the pellet of PAA-coated UCNPs was dispersed in 0.5 mL of DMSO, giving a concentration of *ca.* 24 mg mL^{-1}. A volume of 40 μL PAA-UCNPs in DMSO was transferred to 0.8 mL water for *Z*-potential measurements. Successful PAA coating of UCNPs was confirmed by a negative *Z*-potential value (−21 mV and −22 mV for CS1 and CS2, respectively, Fig. S1 in ESI†). The carboxylic acid groups contained in the PAA coating that provided this negative *Z*-potential value will be activated by EDC/sulfo-NHS for further PEI functionalization *via* amide bond. DLS measurements (Fig. S2 in ESI†) showed that the hydrodynamic sizes of PAA-coated UCNPs were 47 nm for CS1 and 68 nm for CS2, indicating colloidal stability and absence of aggregation.

2.5 EDC/NHS coupling method for dye-functionalized UCNPs

EDC activates carboxyl groups of PAA-coated UCNPs to form a highly reactive and unstable *O*-acylisourea intermediate which reacts with primary amines of polyethylenimine (PEI) to form amide bonds. A more stable ester can be formed upon the addition of sulfo-NHS. Thus, 12 mg of PAA-capped UCNPs in 0.5 mL of DMSO (for both samples; CS1 and CS2) were activated with EDC·HCl (2 mg) and sulfo-NHS (3 mg) for 20 min in order to form the succinimidyl ester, and kept under shaking. PEI (100 mg) in DMSO (3 mL) was then added to the reaction, and the solution was kept under stirring for 10 min. After that, the UCNPs were gradually mixed with 20 μL of DIPEA and left stirring overnight at room temperature. DIPEA was used to keep the system basic enough so that the primary amine remains reactive and the coupling proceeds efficiently. After one day of incubation at room temperature, the reaction was quenched by adding 25 μL of ethanolamine. The PEI-conjugated UCNPs were split into four Eppendorf tubes, and washed with 1 mL of DMSO in each Eppendorf tube by centrifuging at 12 000 rpm for 20 minutes (this process was repeated four times). Finally, the pellet of PEI-coated UCNPs were redispersed in 0.5 mL of DMSO, giving an UCNPs concentration of *ca.* 20 mg mL^{-1}. A volume of 40 μL PEI-coated UCNPs in DMSO was transferred to 0.8 mL water for *Z*-potential measurements.

The *Z*-potential of PEI-coated UCNPs became positive (+30 mV for CS1, and +29 mV for CS2, see Fig. S1 in ESI†), confirming the presence of amine groups on the surface of UCNPs, which will enable the formation of an amide bond between UCNPs and Cy3-NHS (see Fig. S1 in ESI†). The next step was to add 25 μL of DIPEA to the UCNPs and keep stirring for 15 min. Then, 20 μL of dye cyanine3-NHS in DMSO at 1 mg mL^{-1} was poured and kept under stirring at room temperature overnight. In order to improve the binding efficiency between UCNPs-PAA-PEI and Cy3-NHS, 2 mg of EDC and 3 mg of sulfo-NHS were added to the solution and vortexed. Then, the solution was split into two Eppendorf tubes, and washed with 1 mL of DMSO in each Eppendorf tube by centrifugation at 12 000 rpm for 20 minutes (the process was repeated three times). Finally, the pink pellet of UCNPs-PAA-PEI-Cy3 was redispersed in 200 μL of DMSO and stored at 4 °C in the dark to avoid photobleaching.

2.6 Morphological characterization

TEM images were acquired using a JEOL JEM 1010 working at 100 kV and a GATAN Megaview II digital camera. Samples were prepared by depositing a drop of UCNP dispersion onto Formvar-coated copper grids and dried at room temperature.

2.7 Optical characterization

Luminescence lifetimes were determined using the time-resolved photon counting technique with a custom-built fluorescence system previously described in the literature[13] (see Fig. S3 in ESI†). A 967 nm pigtailed 10 W continuous wave (CW) excitation laser (JDSU, L4-9897603), regulated by current and temperature controllers (ILX Lightwave, LDX-36025-12, and LDT-5525B, respectively), emits a beam that passes through a long-pass dichroic filter (Semrock, FF757-Di01). The filtered beam is then focused onto a micro-cuvette (Hellma 101.015-QS, 3 mm optical path) using a 10× objective. The emitted luminescence is redirected by the dichroic mirror towards a short-pass filter (Semrock, FF01-775/SP), which efficiently removes reflected radiation within the 770–1050 nm range. The light is subsequently coupled into an optical fiber leading to a monochromator (Horiba Jobin Yvon, iHR320), which is equipped with an 1800 grooves per mm grating blazed at 500 nm and a photomultiplier tube (Hamamatsu, R928) for upconversion luminescence detection. The signal collected by the photomultiplier tube is connected to a 50 Ohm input of a digital oscilloscope (Agilent, DSO9104A). The trigger for the oscilloscope is provided by the signal from the laser controller. The current laser controller produces excitation pulses ranging from 40 μs to the millisecond scale. The laser's rise and fall times are significantly shorter than the measured UCL decay times, with a nominal value below 10 μs. A custom-developed Matlab program processes each acquired signal in real-time, simulating both the discriminator and the multichannel counter.[40] By analyzing over 2500 trigger signals, a luminescence decay curve is reconstructed.

The luminescence lifetime is extracted by fitting the decay curves to a single exponential function. The fitting procedure considers a time window from t_{ini} to t_{end}, where t_{end} is selected to be sufficiently long to capture the complete luminescence decay (typically t_{end} = 2–2.5 ms). For each experimental decay curve, approximately 15 fits are performed, systematically varying t_{ini} within the interval where the luminescence intensity decreases from 85% to 75% of its maximum value. Further details on this procedure can be found in section S4 of the ESI.† This approach yields an average luminescence lifetime along with its standard error.

To determine the laser intensity (irradiance) at the sample, the laser power was measured using a thermal sensor power meter (Thorlabs, S310C), and the beam spot size was determined using the knife-edge technique,[41] yielding a beam radius of 120 μm (HWHM). Further details are provided in section S5 of the ESI.†

We conducted two set of time-resolved experiments: the first involved varying the excitation pulse width, and the second involved varying the excitation laser power, and consequently the irradiance. Detailed experimental information regarding the excitation conditions used in these studies can be found in section S6 of the ESI.†

Luminescence emission spectra were collected for each set of core–shell nanoparticles, CS1 and CS2, both with and without Cy3 dye bound to their surface, using the CW mode for the excitation laser. Multiple spectra were recorded for each sample, and those spectra were normalized in the red band region. An average intensity was calculated by integrating the area within the green emission band, with the standard deviation used as the error.

3 Results and discussion

Highly monodisperse β-$NaYF_4$:$Yb_{0.2}$ UCNPs with an average diameter of (32 ± 2) nm were synthesized *via* a high-temperature thermal co-precipitation method (see TEM image in Fig. 1A). These initially synthesized β-$NaYF_4$:$Yb_{0.2}$ nanoparticles were subsequently employed as cores for the seed-mediated epitaxial growth of $NaYF_4$:$Yb_{0.2}$,$Er_{0.02}$ active-shells with two different thicknesses. TEM images in Fig. 1B and C confirm the successful formation of core–shell structures and show the increase in particle size due to the growth of the $NaYF_4$:Yb,Er active shell around the β-$NaYF_4$:Yb core. The resulting core–shell nanoparticles exhibit final diameters of (43 ± 3) nm for the sample with a molar ratio of 0.25/0.5 relative to the total amount of RE content in the core synthesis step to the shell growth step (CS1), and (60 ± 3) nm for the sample with a RE molar ratio of 0.25/1 (CS2). These correspond to shell thicknesses of approximately 5.5 nm and 14 nm, respectively, as shown in the size distribution in Fig. 1D. Fig. 1E shows the green and red UCL emission spectrum of a $NaYF_4$:Yb,Er@PAA-PEI UCNPs dispersion in DMSO at a concentration of 0.5 mg mL^{-1}, the concentration used in all reported experiments, upon excitation with a 967 nm CW laser. This emission features two peaks in the green region at approximately 525 nm and 540 nm, corresponding to the $^2H_{11/2} \rightarrow {}^4I_{15/2}$ and $^4S_{3/2} \rightarrow {}^4I_{15/2}$ transitions, respectively, and a red emission band centered around 655 nm, associated with the $^4F_{9/2} \rightarrow {}^4I_{15/2}$ transition. The energy level diagram of the system is depicted in Fig. 1F, highlighting the green upconversion mechanism, which is primarily driven by energy transfer (ET) from Yb^{3+} ions to Er^{3+} ions. As shown in Fig. 1E, the absorption spectrum of Cy3 (blue dashed line) exhibits strong spectral overlap with the green emission band of the UCNP donor, while its fluorescence (light brown dashed line) remains well separated from both the green and red UCL emission. This spectral overlap can be quantitatively evaluated using the spectral overlap integral J:

$$J = \int_{\Delta\lambda} F_D(\lambda)\varepsilon_A(\lambda)\mathrm{d}\lambda, \quad (1)$$

where $F_D(\lambda)$ is the normalized UCL emission spectrum of the UCNP donor (with unit area), and $\varepsilon_A(\lambda)$ is the molar extinction coefficient of the Cy3 acceptor, which typically reaches a maximum value of approximately 1.5×10^5 M^{-1} cm^{-1}. The integration is performed over the selected spectral range $\Delta\lambda$ corres-

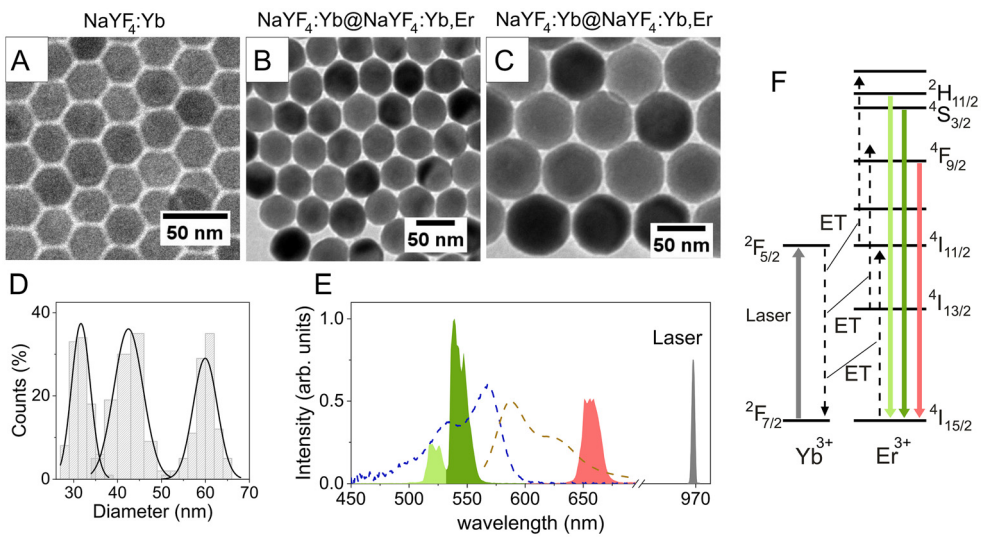

Fig. 1 (A) TEM image of the 32 nm β-$NaYF_4$:$Yb_{0.20}$ core and β-$NaYF_4$:Yb@$NaYF_4$:$Yb_{0.20}$,$Er_{0.02}$ core–shell nanoparticles with different shell thicknesses: CS1, 5.5 nm (B) and CS2, 14 nm (C). (D) Size distribution of core (32 ± 2) nm, and core–shell nanoparticles: CS1 (43 ± 3) nm, and CS2 (60 ± 3) nm, depicted in Fig. A, B, and C, respectively. (E) Green and red UCL emission spectrum of a $NaYF_4$:Yb,Er UCNPs dispersion in DMSO at a concentration of 0.5 mg mL^{-1} and excitation laser spectrum for a 967 nm CW laser power of 0.3 W (633 W cm^{-2}). Dashed lines show the absorption (left curve) and luminescence emission (right curve) spectra of the Cy3 dye FRET pair acceptor. (F) Energy level diagram for Yb^{3+} and Er^{3+} ions describing the processes that give rise to green and red UCL emission bands. The black dashed lines represent the Yb–Er energy transfer (ET) mechanism, whereas the green and red solid lines represent the two green and one red emissions, centered around 525 nm, 540 nm, and 655 nm, respectively.

ponding to the donor emission band (505–575 nm) (see Fig. S6 in ESI†). Based on this, we obtained a spectral overlap integral of $J = 7 \times 10^{15}$ M^{-1} cm^{-1} nm^4, which enabled us to estimate the Förster distance R_0. This characteristic distance is defined as the donor–acceptor separation at which 50% of the donor ions decay *via* energy transfer to the Cy3 acceptors, that is, the distance at which the energy transfer rate equals the intrinsic donor decay rate in the absence of acceptor. R_0 is given by:

$$R_0 = 0.0211(\kappa^2 \eta_D n^{-4} J)^{1/6} \text{ [nm]}. \quad (2)$$

The factor κ^2 accounts for the relative orientation of the donor and acceptor dipole moments. It is commonly assumed to be 2/3, which corresponds to the condition of dynamic isotropic averaging. η_D represents the intrinsic quantum yield of the donor in the absence of the acceptor, that is, the quantum yield of the excited state of the Er^{3+}.[42] According to Bhuckory *et al.*,[42] this value has been estimated to lie between 20% and 30% based on FRET measurements in UCNPs with different core–shell architectures. In our calculations, we used $\eta_D = 0.25$. The parameter n denotes the refractive index of the medium surrounding the FRET pair, we used the value for the host matrix $NaYF_4$, $n = 1.48$.[43] By evaluating eqn (2) with these parameters, we obtained a theoretical Förster distance of $R_0 \approx 5.3$ nm. In order to assess the robustness of this estimation, we analyzed the effect of uncertainties in the parameters involved. According to the Förster distance expression (eqn (2)), the parameter that potentially induces the largest variation in R_0 is the refractive index n, due to its dependence to the fourth power. The relative variation can be approximated by $\Delta R_0/R_0 = (4/6)\Delta n/n$. The refractive index may vary between that of the solvent (1.33) and that of the host matrix (1.5), leading to a relative variation of approximately 7.7%, which translates into an uncertainty of about 0.4 nm in the Förster distance. Although the remaining parameters in eqn (2) contribute less significantly to the overall uncertainty, the intrinsic quantum yield η_D is the most difficult to constrain. It could reasonably vary between 15% and 35%, resulting in a relative variation of $\Delta R_0/R_0 = (1/6)\Delta\eta_D/\eta_D \approx 13\%$, which implies an additional uncertainty in R_0 of about 0.7 nm. In summary, considering these uncertainties, the Förster distance R_0 is expected to lie within the range of approximately 4.5 to 6.5 nm. This result suggests that, in core–shell nanoparticles with a 5.5 nm active shell (CS1), a significant fraction of the Er^{3+} ions is likely to undergo efficient energy transfer to Cy3 acceptors. Consequently, a measurable FRET efficiency is expected in these nanoparticles (CS1).

In order to determine the FRET efficiency under steady-state conditions, we measured the emission spectra of the sample CS1 with and without the attached Cy3 (Fig. 2A). The relative intensity decrease in the green UCL of UCNPs with acceptor molecules, compared to those without Cy3, quantifies the magnitude under investigation. This value is determined using the following expression:

$$E_{FRET} = 1 - \frac{I_{DA}}{I_D}, \quad (3)$$

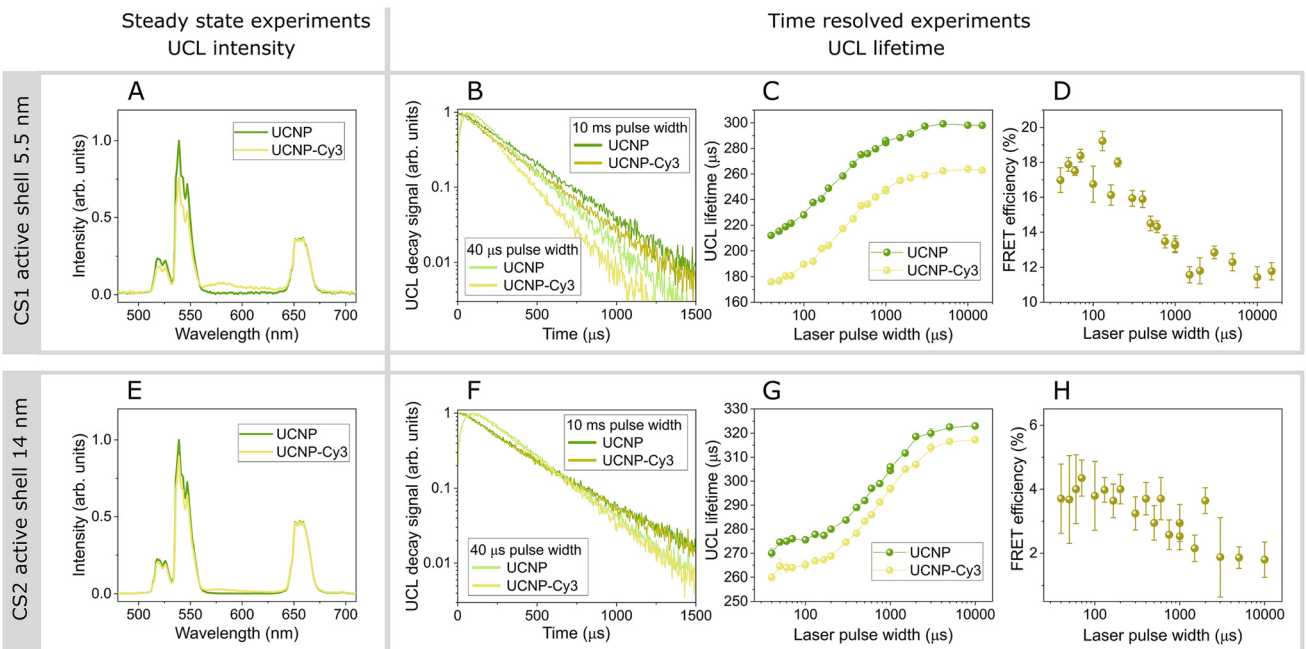

Fig. 2 (A) Green UCL emission spectra for a DMSO $NaYF_4$:Yb,Er UCNPs dispersion (0.5 mg mL^{-1}) (with and without Cy3) under 967 nm CW irradiation of 0.2 W (444 W cm^{-2}). (B) Green (540 nm) UCL decay curves for two extreme representative excitation pulse widths (40 μs and 10 ms) in the case with and without Cy3, using an excitation laser power of 2.2 W (5 kW cm^{-2}). (C) Green UCL lifetime as a function of the excitation pulse width for the sample with and without Cy3. Here, error bars are present but not discernible due to being smaller than the data point symbols. (D) FRET efficiency calculated from data of figure (C). (E)–(H) same as (A)–(D) for the UCNPs with 14 nm active shell thickness.

where I_D and I_{DA} are the spectra intensity of the UCNPs in the absence and presence of the acceptor, respectively. The intensities were calculated by integrating the spectra over the 510 to 565 nm range. Based on these data, we calculated a FRET efficiency of 29%. This relatively high value suggest a strong interaction between the donor and acceptor, as expected from the favorable spectral overlap and spatial proximity provided by the relatively thin active shell. However, as noted in the Introduction, conclusive evidence that the observed luminescence quenching results from a FRET mechanism, as opposed to other processes such as reabsorption or scattering, comes from time-resolved measurements. Specifically, FRET induces a reduction in the donor's luminescence lifetime due to the addition of a non-radiative decay pathway. To verify this, we measured the UCL decay curves of the UCNPs in the presence and absence of Cy3 acceptors using a custom-built experimental setup (Fig. S3 in ESI†). These measurements allow us to estimate the FRET efficiency using the following expression:

$$E_{FRET} = 1 - \frac{\tau_{DA}}{\tau_D}, \quad (4)$$

where τ_D is the lifetime of the donor UCNP, and τ_{DA} is the lifetime of the donor nanoparticle in the presence of the acceptor molecules. A reasonable concern arises regarding this approach. As discussed in the Introduction, recent studies have introduced a new paradigm in the interpretation of UCL decay, showing that the measured luminescence lifetime can depend strongly on the excitation pulse width.[35] Therefore, our hypothesis is that the FRET efficiency obtained from lifetime measurements may also be affected by the duration of the excitation pulse, potentially leading to a biased estimation of the energy transfer efficiency depending on the experimental conditions.

To experimentally validate this hypothesis, we investigated the dependence of FRET efficiency on the excitation laser pulse width. Specifically, we measured the UCL decay curves of the green emission band (at 540 nm) using a 967 nm laser, varying the pulse duration across a wide temporal window, ranging from microseconds to milliseconds, in order to probe excitation conditions below and above the typical UCL lifetime. The pulse repetition rate was adjusted to allow complete relaxation of the ions to the ground state before the next excitation pulse (see experimental details in section S6 in ESI†). Fig. 2B presents representative decay curves obtained under short (40 μs) and long (10 ms) excitation pulses. In both cases, a noticeably faster decay is observed in the presence of Cy3, indicating effective energy transfer regardless of the pulse regime. The UCL lifetimes were determined by fitting the decay curves with a single-exponential model, using different fitting ranges as described in subsection 2.7. Fig. 2C summarizes the extracted UCL lifetimes as a function of the excitation pulse width, in both the absence and presence of Cy3. In both cases, the lifetime initially increases with pulse duration before reaching a plateau at longer pulses.

This plateau suggests that the population of excited states has reached saturation. This behavior is further supported by the full rise-and-decay UCL signals shown in Fig. S7 in ESI,† where the signal rise flattens, indicating that the system approaches a steady-state population during long excitation pulses.

On the other hand, we have confirmed that the energy transfer from the UCNP to Cy3 gives rise to a slower decay component in the Cy3 emission at 582 nm, which otherwise would typically be in the nanosecond range (more details in section S9 in ESI†). From the lifetime values of Fig. 2C, the FRET efficiency was calculated and is shown in Fig. 2D. The results reveal a clear dependence of the FRET efficiency on the excitation pulse width, with maximum values close to 20% observed under short-pulse excitation, gradually decreasing to approximately 10% as the pulse duration increases, corresponding to a 50% reduction in apparent FRET efficiency. Kotulska *et al.* reported UCL lifetime for similar UCNPs with and without an attached acceptor of 95 μs and 163 μs for a 10 ns pulse width, and 173 μs and 175 μs for a 4 ms pulse width, resulting in FRET efficiencies of 41.7% and 1.2%, respectively. They also reported a FRET efficiency under steady-state conditions of 89%.[37] In addition to the observed dependence of FRET efficiency on the excitation pulse width, none of the extracted values seem to approach the actual FRET efficiency measured from the steady-state emission spectra. This observation highlights a fundamental limitation: accurately quantifying the true contribution of FRET is not feasible through UCL lifetime analysis alone, as the decay rate change induced by FRET in the green emission level cannot be reliably obtained through the change in the UCL lifetime. This systematic underestimation of the FRET efficiency, and thus of the FRET rate, has significant implications for the field of UCNP-based FRET sensors, potentially leading to a substantial reduction in their achievable detection sensitivity.

Furthermore, if the FRET efficiency determined from steady-state spectral measurements is low, the associated changes in the donor lifetime may become too subtle to be detected. Indeed, there are reports in the literature where no measureable difference in the donor lifetime was observed, despite clear evidence of FRET through spectral intensity changes.[38] To further corroborate this point, we synthesized a second batch of UCNPs featuring a much thicker active shell of $NaYF_4$:$Yb_{0.2}$,$Er_{0.02}$, with a thickness of approximately 14 nm. In these core–shell nanoparticles, a substantial fraction of Er^{3+} ions are expected to be located too far from the Cy3 acceptors to enable significant energy transfer, resulting in an overall lower FRET efficiency. To experimentally verify this, we first measured the UCL spectra of these nanoparticles in the presence and absence of Cy3, as shown in Fig. 2E, obtaining a steady state measurement of FRET efficiency corresponding to 10%. In this situation, the UCL decay curves measured under pulsed excitation are very similar in the absence and presence of Cy3, as shown in Fig. 2F. The UCL lifetime values exhibit a similar dependence on the excitation pulse width as previously observed for the UCNPs with thinner active shell, however, the decay curves for the samples with and without Cy3 are now much closer to each other (see Fig. 2G). As a result, the FRET efficiency achieved for these larger-shell nanoparticles (CS2) is substantially lower than that observed for the CS1 nanoparticles. In fact, the maximum FRET

efficiency, reached under short-pulse excitation, is about 4%, progressively decreasing to below 2% as the pulse duration increases. Notably, at longer pulse widths, the differences between the lifetimes measured with and without Cy3 become almost indistinguishable, falling within the range of experimental uncertainty, thus making it extremely challenging to detect any FRET contribution through lifetime measurements.

Next, to gain a deeper understanding of the excitation-dependent FRET efficiency in UCNP systems, we expanded our study by varying not only the excitation pulse width but also the excitation laser power. UCL decay curves were analized as a function of laser power, varied from 0.3 W to 5.6 W, corresponding to an irradiance range of 663 W cm^{-2} to 12.3 kW cm^{-2}, with a fixed pulse width of 750 μs (see experimental details in section S6 in ESI†). In Fig. 3A, we plotted the UCL lifetime as a function of laser irradiance, both with and without Cy3 acceptors. As expected, the UCL lifetime increases with laser irradiance in both cases. In addition, the corresponding FRET efficiency shows a clear variation with laser irradiance, ranging from 15% to 11% (see Fig. 3B). This increase in lifetime with irradiance is in line with results from our previous work,[35] and from other authors that have reported an increase in the UCL lifetime of the 540 nm emission (i) for powder $NaLuF_4$:$Yb_{0.9}$,$Er_{0.02}$ microrods when increasing excitation irradiance from 3 W cm^{-2} to 25 W cm^{-2} and using pulses up to 1 ms width,[33] and (ii) for drop-casted 8 nm $NaYF_4$:$Yb_{0.2}$,$Er_{0.02}$ cores with 4 ms excitation pulses within 0.01–1 kW cm^{-2} irradiance.[32] This behavior may be explained due to the increasing population of Er^{3+} intermediate states (*e.g.*, the metastable $^4I_{13/2}$ level) at higher irradiances, which results in a slower decay time of the 540 nm emission compared with low irradiances.[35] Although an opposite behavior or barely any change with irradiance has also been reported,[30,32] we believe that this can be ascribed to the use of different Yb^{3+}/Er^{3+} ratio and dopant concentrations, studied excitation range, nanoparticle size, structure/ion distribution (*e.g.* core@shell) and state of sample (dried *vs.* dispersed), which can result in different contributions to the temporal dynamics of the population of Er^{3+} levels by energy transfer, cross-relaxation and energy migration between Ln^{3+} ions, as well as variable surface and temperature quenching effects.

In our case, it is also interesting to highlight that experiments from Fig. 2C and 3A involving variations in excitation pulse width and irradiance, can be collapsed into a single master curve when plotting the UCL lifetime as a function of laser fluence, *i.e.*, the product of irradiance and pulse duration (see Fig. 3C). This confirms that the laser fluence determines the population of the system at the moment when the excitation pulse ends, ultimately influencing the subsequent UCL decay and, as result, its lifetime. Therefore, the same behavior must be observed when representing the corresponding FRET data, as indeed is confirmed in Fig. 3D.

These findings underscores the importance of exercising caution when comparing FRET efficiencies obtained under different excitation conditions, as both excitation pulse width and irradiance can significantly influence the UCL lifetime, and consequently, the measured FRET efficiency in UCNP-based FRET systems.

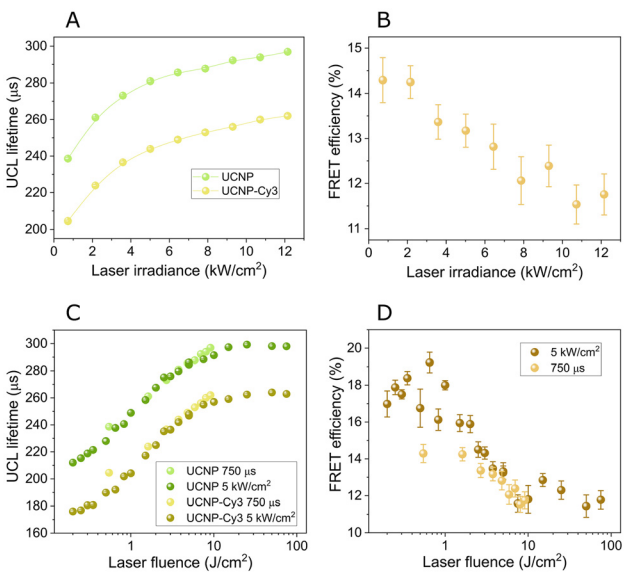

Fig. 3 (A) UCL luminescence lifetime as a function of laser irradiance for CS1 core–shell nanoparticles (with active shell 5.5 nm) with and without dye for a fixed pulse width of 750 μs. Error bars are included but not visible as they are smaller than the symbol size. (B) FRET efficiency obtained from data shown in A. (C) UCL lifetime extracted from Fig. 2C (dark-colored symbols) and A (light-colored symbols) as a function of laser fluence, measured by varying the laser pulse width and laser power, respectively. (D) FRET efficiency calculated from the UCL lifetime data shown in C.

3.1 Theoretical interpretation

To better understand the experimental findings, we conducted a rate equation analysis aimed at qualitatively reproducing the observed results. This analysis allowed us to demonstrate that the variation in FRET efficiency as function of laser pulse width and irradiance is a dynamic phenomenon inherently linked to the upconversion process. To achieve this, we employed the following rate equation model:

$$\begin{aligned}
\frac{dN_{Er1}}{dt} &= -W_{Er10}N_{Er1} + W_{Er21}N_{Er2} \\
&\quad - K_3N_{Er1}N_{Yb1} - 2C_{Er1}{N_{Er1}}^2, \\
\frac{dN_{Er2}}{dt} &= -(W_{Er20} + W_{Er21})N_{Er2} + W_{Er32}N_{Er3} \\
&\quad + K_2N_{Er0}N_{Yb1} - K_{B2}N_{Er2}N_{Yb0} - K_4N_{Er2}N_{Yb1} \\
&\quad + C_{Er1}{N_{Er1}}^2 - 2C_{Er2}{N_{Er2}}^2 \\
\frac{dN_{Er3}}{dt} &= -(W_{Er30} + W_{Er32})N_{Er3} + W_{Er43}N_{Er4} + K_3N_{Er1}N_{Yb1}, \quad (5) \\
\frac{dN_{Er4}}{dt} &= -(W_{Er40} + W_{Er43} + W_{Er4FRET})N_{Er4} \\
&\quad + K_4N_{Er2}N_{Yb1} + C_{Er2}{N_{Er2}}^2 \\
\frac{dN_{Yb1}}{dt} &= -W_{Yb}N_{Yb1} + \frac{1}{2}W_{Yb}\frac{I}{I_{sat}}(N_{Yb0} - N_{Yb1}) \\
&\quad - K_2N_{Er0}N_{Yb1} + K_{B2}N_{Er2}N_{Yb0} \\
&\quad - K_3N_{Er1}N_{Yb1} - K_4N_{Er2}N_{Yb1}.
\end{aligned}$$

The term N_{Erj} represents the density of Er^{3+} ions in the energy level j, where the subscripts j = 0, 1, 2, 3, 4 correspond to energy levels $^4I_{15/2}$, $^4I_{13/2}$, $^4I_{11/2}$, $^4F_{9/2}$, and $^4S_{3/2}$ of Er^{3+}, respectively (see Fig. 4A). The populations of fast-decaying levels such as $^4F_{7/2}$ and $^4I_{9/2}$ are neglected, while the populations of $^2H_{11/2}$ and $^4S_{3/2}$ are assumed to be in thermal equilibrium. The total Er^{3+} ion density in the nanoparticle is given by the sum $N_{Er0} + N_{Er1} + N_{Er2} + N_{Er3} + N_{Er4} = N_{Er}$. Similarly, the densities of Yb^{3+} ions in the $^2F_{7/2}$ and $^2F_{5/2}$ energy levels are denoted as N_{Yb0} and N_{Yb1}, respectively, with their total density expressed as $N_{Yb0} + N_{Yb1} = N_{Yb}$. The decay rate from level j to level l of Er^{3+} is represented by W_{Erjl}. Decay from an excited level to the ground state (W_{Erj0}) is considered radiative (on the millisecond range), whereas decay to the next lower excited level occurs *via* faster nonradiative multi-phonon relaxation (on the microsecond scale). The decay rate from the excited state to the ground state of Yb^{3+} is denoted as W_{Yb}. The coefficients K_2, K_3, and K_4 describe the resonant energy transfer from the excited Yb^{3+} ions (sensitizers) to levels 2, 3, and 4 of Er^{3+} (activators), respectively. Additionally, K_{B2} represents the back energy transfer coefficient from Er^{3+} in level 2 to Yb^{3+}. The terms C_{Er1} and C_{Er2} correspond to cross-relaxation energy transfer between neighboring Er^{3+} ions. Specifically, C_{Er1} describes the typical quenching mechanism in erbium-doped fiber amplifiers, given by the transition ($^4I_{13/2}$, $^4I_{13/2}$) → ($^4I_{15/2}$, $^4I_{9/2}$), while C_{Er2} corresponds to an upconversion energy transfer leading to green emission, ($^4I_{11/2}$, $^4I_{11/2}$) → ($^4I_{15/2}$, $^4F_{7/2}$). All of the above processes are illustrated in the energy level diagram shown in Fig. 4A. Finally, the excitation laser intensity (irradiance) is denoted as I (in W cm^{-2}), which can be normalized by the saturation intensity $I_{sat} = \hbar\omega W_{Yb}/(2\sigma_{Yb})$ of the Yb^{3+} $^2F_{7/2}$ → $^2F_{5/2}$ transition. Here, σ_{Yb} is the absorption (approximately equal to the emission) cross-section at the laser wavelength, and $\hbar\omega$ represents the transition energy, which is resonant with the excitation laser wavelength. For the simulations, we initially set the decay rates, energy transfer coefficients, and other physical parameters to values comparable to those reported in the literature.[35,44–47] We then refined these parameters to better align with our experimental results for the CS1 UCNPs (see section S10 in ESI†).

To theoretically study the time evolution of the populations, we modeled the excitation intensity as a square pulse with a given amplitude I/I_{sat} and pulse width, matching the experimental conditions. At the initial time t = 0, when the laser is switched on, all ions are assumed to be in their ground state, with no population in the excited levels. Thus, the initial conditions for the simulations at t = 0 are $N_{Er1} = N_{Er2} = N_{Er3} = N_{Er4} = N_{Yb1} = 0$, while $N_{Er0} = N_{Er}$ and $N_{Yb0} = N_{Yb}$. Eqn (5) was numerically solved using an explicit Runge–Kutta method implemented in Matlab.[48] In particular, the time evolution of the N_{Er4} population after the laser is turned off defines the UCL decay curve of the green emission band. The simulated decay curves were fitted following the same procedure as the experimental data to extract the simulated lifetime.

The decay rate $W_{Er4FRET}$ in eqn (5) represents the resonant energy transfer process from the Er^{3+} ions in the $^4S_{3/2}$ excited

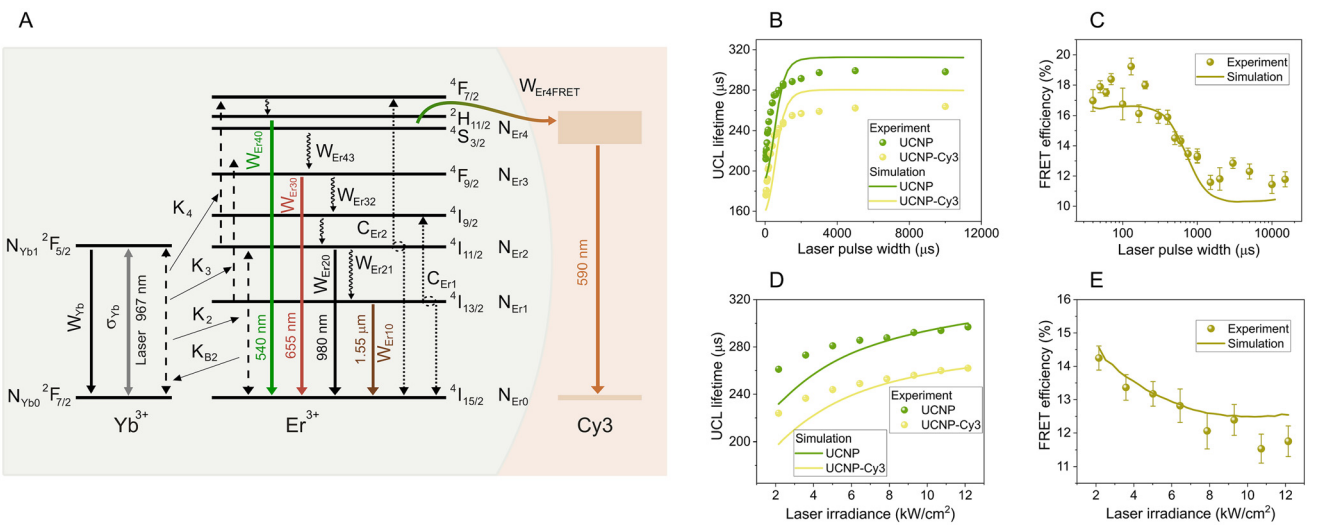

Fig. 4 (A) Energy level diagram for Yb^{3+} and Er^{3+} ions describing all the physical processes used in the rate equation model. Black dashed lines represent the Yb–Er ET mechanism (K_2, K_{B2}, K_3, K_4), whereas black dotted lines represent Er–Er ET mechanisms (C_{Er1} and C_{Er2}). Gray solid line represents ground state absorption and stimulated emission of Yb^{3+} ions (σ_{Yb1}). The remaining solid lines represent radiative decay rates from different levels (W_{Yb1} for Yb^{3+} and W_{Er1}, W_{Er20}, W_{Er30}, W_{Er40} for Er^{3+}), whereas faster nonradiative decay rates are represented by wavy lines (W_{Er43}, W_{Er32}, W_{Er21}). We also show the FRET rate $W_{Er4FRET}$ from the UCNP donor to the Cy3 acceptor, as well as the decay of the Cy3 emission. (B) Simulated green UCL lifetime, calculated from decay curve of N_{Er4}, as a function of the excitation pulse width for both with ($W_{Er4FRET}$) and without ($W_{Er4FRET}$ = 0) Cy3 acceptors (solid lines). Experimental results from Fig. 2C are added for comparison purposes (symbols). (C) Simulated (solid line) and experimental (symbols) FRET efficiency calculated from the results shown in B. (D) Simulated green UCL lifetime, calculated from decay curve of N_{Er4}, as a function of laser irradiance for both with ($W_{Er4FRET}$) and without ($W_{Er4FRET}$ = 0) Cy3 acceptors (solid lines). Experimental results from Fig. 3A are added for comparison purposes (symbols). (E) Simulated (solid line) and experimental (symbols) FRET efficiency calculated from the results shown in D.

state to Cy3 acceptor molecule (see Fig. 4A). This parameter quantifies how efficiently energy is transferred from the UCNP donor to Cy3, thereby reducing the population of the $^4S_{3/2}$ state *via* the FRET mechanism. By incorporating $W_{Er4FRET}$ into the total decay rate of this energy level, the model accounts for the presence of the acceptor and its impact on the UCL emission. Conversely, to simulate the behavior of the UCNPs in the absence of Cy3, we simply set $W_{Er4FRET} = 0$, effectively removing the energy transfer contribution. This allows for a direct comparison between the UCL lifetime with and without Cy3.

Based on the experimental results, we assumed a FRET efficiency of $E_{FRET} = 29\%$ as determined from steady-state measurements of the CS1 UCNPs. This efficiency can be expressed in terms of the intrinsic decay rates as:

$$E_{FRET} = \frac{W_{Er4FRET}}{W_{Er40} + W_{Er43} + W_{Er4FRET}}. \quad (6)$$

Eqn (6) allowed us to estimate the FRET decay rate $W_{Er4FRET}$ (see section S10 in ESI†). Fig. 4B presents the simulated UCL lifetime, calculated from decay curve of N_{Er4}, as a function of laser pulse width, both in the presence and absence of Cy3. The FRET efficiency calculated from these simulated curves is shown in Fig. 4C. In both figures, the experimental data are included for comparison purposes. A good qualitative agreement is observed between the simulated and experimental results, indicating that the model successfully captures the key dynamics of the system. This confirms that the dependence of FRET efficiency on laser pulse width is an intrinsic dynamic process, directly tied to the intrincate interplay governing the UCL lifetime behavior. The competition between different pathways, including radiative and non-radiative relaxation, energy transfer between ions, and resonant energy transfer to Cy3, dynamically influences the UCL lifetime, leading to variations in the observed FRET efficiency as a function of excitation parameters. To further investigate this behavior, we extended our simulations to analyze the variation of FRET efficiency with laser irradiance. Fig. 4D shows the simulated UCL lifetime for both cases, with and without Cy3, while Fig. 4E presents the corresponding FRET efficiency. Once again, a reasonable qualitative agreement with the experimental data is observed, reinforcing the validity of our model.

An important trend emerges from these simulations: as the laser fluence increases, either by increasing the pulse width or by raising the laser irradiance, the overall UCL lifetime also increases. This lengthening of the UCL lifetime reduces the relative impact of the absolute lifetime change caused by FRET. Moreover, even at short laser pulse widths, the FRET efficiency remains below 20% (see Fig. 4C) failing to reach the 29% observed in steady-state measurements. To theoretically validate this discrepancy, we analyzed FRET under steady-state conditions using CW laser excitation. In this scenario, we calculated the steady-state population of the green emission level, N_{Er4}, which is directly proportional to its emission intensity. This approach allowed us to determine the FRET efficiency under continuous excitation and compare it with the transient case. The reduction in the steady-state population N_{Er4} upon introducing the acceptor resulted in a FRET efficiency close to 29%, consistent with the value predicted by eqn (6) and in agreement with steady-state FRET experiments.

That means that in steady-state simulations, introducing a FRET decay channel that accounts for 29% of the total decay rate from the green-emitting level results in a corresponding 29% reduction in its stationary population. This behavior aligns with expectations, as the steady-state UCL intensity directly reflects the balance between excitation and all deactivation pathways, including the added FRET process. Specifically, the green UCL intensity is governed by the quantum yield of the emitting level, expressed as the ratio of its radiative decay rate to the total decay rate. Thus, any increase in the total decay rate due to FRET results in a proportional decrease in the UCL intensity. However, this proportionality does not hold in time-resolved simulations. In these cases, the measured UCL lifetime does not directly correspond to the inverse of the total decay rate of the emitting level, *i.e.*, $1/W_{Er4}$. This discrepancy arises because the UCL lifetime is determined not only by the decay of the green-emitting level, but also by the entire dynamic upconversion process. It incorporates multiple coupled processes, including sensitizer–activator energy transfer (K_2, K_3, K_4, K_{B2}), relaxation rates of intermediate states, and cross-relaxation pathways among Er^{3+} ions (C_{Er1}, C_{Er2}), all occurring on different timescales and dynamically influencing the UCL lifetime. As a result, while FRET modifies the decay rate of the emitting level in a defined way, this change is only partially reflected in the measured UCL lifetime. The UCL decay represents a convolution of the full kinetic network, meaning that lifetime-based assessments of FRET efficiency may systematically underestimate the true contribution of the FRET process.

4 Conclusions

In this study, we systematically investigated the influence of excitation conditions, specifically laser pulse width and laser power (and irradiance), on the quantification of FRET efficiencies in UCNP-based systems, addressing the common assumption that time-resolved measurements are gold standard for probing FRET. To this end, we synthesized core–shell β-$NaYF_4$:$Yb_{0.2}$@$NaYF_4$:$Yb_{0.2}$,$Er_{0.02}$ UCNPs with two distinct active shell thicknesses: a thin 5.5 nm shell designed to promote strong donor-to-Cy3 acceptor interactions, achieving a FRET efficiency of 29% as determined by steady-state measurements, and a thicker 14 nm active shell aimed at reducing energy transfer efficiency (10% from steady-state measurements).

Through time-resolved upconversion luminescence (UCL) experiments and theoretical modeling, we demonstrated that both excitation pulse width and laser irradiance have a significant impact on the measured FRET efficiency. For UCNPs with thin active shells, high FRET efficiencies of around 20% were observed under short excitation pulses. However, as the excitation pulse duration increased and/or laser power was raised, the measured FRET efficiency decreased substantially, dropping

to approximately 10% for long excitation pulses. This variation is attributed to the complex dynamics of upconversion systems, where the population of intermediate energy states interferes with the accurate determination of the intrinsic decay time of the emitting level. As a result, the real FRET efficiency cannot be directly inferred from changes in the UCL lifetime alone, highlighting the need to account for these dynamic processes when quantifying FRET in UCNP-based systems.

In the case of UCNPs with thick shells (14 nm), the FRET efficiency assessed *via* lifetime measurements dropped to very small values, within the experimental uncertainty, under long excitation pulses, suggesting no detectable energy transfer. Nevertheless, spectral measurements still revealed a decrease in donor emission and an increase in Cy3 acceptor emission, confirming that FRET was indeed occurring, around 10% FRET efficiency. This highlights that lifetime-based quantification can fail to detect FRET under certain excitation conditions, particularly in systems with low donor–acceptor coupling.

Overall, our findings reveal that FRET efficiency determined through time-resolved luminescence measurements vary with both excitation irradiance and pulse width. Consequently, excitation conditions act as hidden variables that can systematically bias FRET measurements. Even though this drawback is observed in UCNPs, it is likely to be present in other nanosystems with complex dynamics, for example some quantum dots, where nonexponential photoluminescence decay behavior has been found.

Considering all these results, identifying the optimal strategy for accurately assessing FRET efficiency in UCNP-based systems remains challenging. From the perspective of lifetime-based measurements, one should aim to optimize excitation parameters, UCNP structure, doping concentrations, and emission band selection to approach a UCL lifetime that closely reflects the intrinsic decay time of the emitting state. In terms of intensity-based measurements, particular attention must be given to minimizing reabsorption effects, such as by carefully diluting the samples, to ensure that the observed variations are primarily due to FRET. However, it is difficult to definitively claim that no other contributions are influencing the results since intensity-based FRET quantification is highly sensitive to variations in sample concentration (*e.g.*, UCNP concentration before and after the presence of acceptors, sample sedimentation), as well as media characteristic (*e.g.*, scattering, inner filter effect).

Conflicts of interest

There are no conflicts to declare.

Data availability

The dataset for this article, including .dat data files corresponding to the figures in the manuscript, is available at **https://doi.org/10.5281/zenodo.15351352**.

Acknowledgements

This work was supported by Ministerio de Ciencia e Innovación (PID2023-150645OA-I00, PID2021-122806OB-I00, PID2021-123318OB-I00 and TED2021-132317B-I00), Fundación Alonso (2024/0041), and Comunidad de Madrid (P2022/BMD-7403 RENIM-CM). A. C. R. thanks UCM-Santander for a predoctoral contract (CT15/23).

References

1 T. Förster, *Ann. Phys.*, 1948, **6**, 55–75.
2 R. M. Clegg, *Curr. Opin. Biotechnol.*, 1995, **6**, 103–110.
3 K. E. Sapsford, L. Berti and I. L. Medintz, *Angew. Chem., Int. Ed.*, 2006, **45**, 4562–4589.
4 *FRET - Förster Resonance Energy Transfer*, ed. I. Medintz and N. Hildebrandt, John Wiley & Sons, Ltd, 2013.
5 W. R. Algar, N. Hildebrandt, S. S. Vogel and I. L. Medintz, *Nat. Methods*, 2019, **16**, 815–829.
6 L. Stryer and R. P. Haugland, *Proc. Natl. Acad. Sci. U. S. A.*, 1967, **58**, 719–726.
7 D. Nettels, N. Galvanetto, M. T. Ivanovic, M. Nüesch, T. Yang and B. Schuler, *Nat. Rev. Phys.*, 2024, **6**, 587–605.
8 *Principles of Fluorescence Spectroscopy*, ed. J. R. Lakowicz, Springer, New York, 3rd edn, 2006.
9 C. Berney and G. Danuser, *Biophys. J.*, 2003, **84**, 3992–4010.
10 F. Auzel, *Chem. Rev.*, 2004, **104**, 139–174.
11 M. Haase and H. Schäfer, *Angew. Chem., Int. Ed.*, 2011, **50**, 5808–5829.
12 V. Muhr, C. Würth, M. Kraft, M. Buchner, A. J. Baeumner, U. Resch-Genger and T. Hirsch, *Anal. Chem.*, 2017, **89**, 4868–4874.
13 S. Melle, O. G. Calderon, M. Laurenti, D. Mendez-Gonzalez, A. Egatz-Gómez, E. López-Cabarcos, E. Cabrera-Granado, E. Díaz and J. Rubio-Retama, *J. Phys. Chem. C*, 2018, **122**, 18751–18758.
14 L. Francés-Soriano, N. Estebanez, J. Pérez-Prieto and N. Hildebrandt, *Adv. Funct. Mater.*, 2022, **32**, 2201541.
15 F. Pini, L. Francés-Soriano, N. Peruffo, A. Barbon, N. Hildebrandt and M. M. Natile, *ACS Appl. Mater. Interfaces*, 2022, **14**, 11883–11894.
16 F. Pini, L. Francés-Soriano, V. Andrigo, M. M. Natile and N. Hildebrandt, *ACS Nano*, 2023, **17**, 4971–4984.
17 K. Kuningas, H. Päkkilä, T. Ukonaho, T. Rantanen, T. Lövgren and T. Soukka, *Clin. Chem.*, 2007, **53**, 145–146.
18 F. Vetrone, R. Naccache, C. G. Morgan and J. A. Capobianco, *Nanoscale*, 2010, **2**, 1185–1189.
19 S. Jiang and Y. Zhang, *Langmuir*, 2010, **26**, 6689–6694.
20 T. Riuttamäki, I. Hyppänen, J. Kankare and T. Soukka, *J. Phys. Chem. C*, 2011, **115**, 17736–17742.
21 Y. Wang, K. Liu, X. Liu, K. Dohnalová, T. Gregorkiewicz, X. Kong, M. C. G. Aalders, W. J. Buma and H. Zhang, *J. Phys. Chem. Lett.*, 2011, **2**, 2083–2088.

22 N.-T. Chen, S.-H. Cheng, C.-P. Liu, J. S. Souris, C.-T. Chen, C.-Y. Mou and L.-W. Lo, *Int. J. Mol. Sci.*, 2012, **12**, 16598–16623.
23 M. V. DaCosta, S. Doughan, Y. Han and U. J. Krull, *Anal. Chim. Acta*, 2014, **832**, 1–33.
24 Y. Ding, F. Wu, Y. Zhang, X. Liu, E. M. L. D. de Jong, T. Gregorkiewicz, X. Hong, Y. Liu, M. C. G. Aalders, W. J. Buma and H. Zhang, *J. Phys. Chem. Lett.*, 2015, **6**, 2518–2523.
25 Y. Huang, E. Hemmer, F. Rosei and F. Vetrone, *J. Phys. Chem. B*, 2016, **120**, 4992–5001.
26 V. Torres Vera, D. Mendez-Gonzalez, D. J. Ramos-Ramos, A. Igalla, M. Laurenti, R. Contreras-Caceres, E. Lopez-Cabarcos, E. Diaz, J. Rubio-Retama, S. Melle and O. G. Calderon, *J. Mater. Chem. C*, 2021, **9**, 8902–8911.
27 Y. Chai, X. Zhou, X. Chen, C. Wen, J. Ke, W. Feng and F. Li, *ACS Appl. Mater. Interfaces*, 2022, **14**, 14004–14011.
28 J. Bergstrand, Q. Liu, B. Huang, X. Peng, C. Würth, U. Resch-Genger, Q. Zhan, J. Widengren, H. Ågren and H. Liu, *Nanoscale*, 2019, **11**, 4959–4969.
29 T. A. Laurence, Y. Liu, M. Zhang, M. J. Owen, J. Han, L. Sun, C. Yan and G.-y. Liu, *J. Phys. Chem. C*, 2018, **122**, 23780–23789.
30 D. J. Gargas, E. M. Chan, A. D. Ostrowski, S. Aloni, M. V. P. Altoe, E. S. Barnard, B. Sanii, J. J. Urban, D. J. Milliron, B. E. Cohen and P. J. Schuck, *Nat. Nanotechnol.*, 2014, **9**, 300–305.
31 Y. Han, X. Zhang and L. Huang, *Chem. – Eur. J.*, 2023, **29**, e202302633.
32 A. Teitelboim, B. Tian, D. J. Garfield, A. Fernandez-Bravo, A. C. Gotlin, P. J. Schuck, B. E. Cohen and E. M. Chan, *J. Phys. Chem. C*, 2019, **123**, 2678–2689.
33 Y. Han, C. Gao, T. Wei, K. Zhang, Z. Jiang, J. Zhou, M. Xu, L. Yin, F. Song and L. Huang, *Angew. Chem., Int. Ed.*, 2022, **61**, e202212089.
34 Y. Gao, J. Liu, J. Wan, M. Guo, M. Wei, K. Xu, Z. Yuan and X. Xie, *J. Lumin.*, 2024, **266**, 120325.
35 A. Casillas-Rubio, D. Mendez-Gonzalez, M. Laurenti, J. Rubio-Retama, O. G. Calderón and S. Melle, *Nanoscale*, 2024, **16**, 12184–12195.
36 A. Pilch-Wrobel, A. M. Kotulska, S. Lahtinen, T. Soukka and A. Bednarkiewicz, *Small*, 2022, **18**, 2200464.
37 A. M. Kotulska, A. Pilch-Wróbel, S. Lahtinen, T. Soukka and A. Bednarkiewicz, *Light: Sci. Appl.*, 2022, **11**, 256.
38 S. Bhuckory, S. Lahtinen, N. Höysniemi, J. Guo, X. Qiu, T. Soukka and N. Hildebrandt, *Nano Lett.*, 2023, **23**, 2253–2261.
39 D. Mendez-Gonzalez, V. Torres Vera, I. Zabala Gutierrez, C. Gerke, C. Cascales, J. Rubio-Retama, O. G. Calderón, S. Melle and M. Laurenti, *Small*, 2022, **18**, 2105652.
40 T. Stacewicz and M. Krainska-Miszczak, *Meas. Sci. Technol.*, 1997, **8**, 453–455.
41 M. A. de Araújo, R. Silva, E. de Lima, D. P. Pereira and P. C. de Oliveira, *Appl. Opt.*, 2009, **48**, 393–396.
42 S. Bhuckory, E. Hemmer, Y.-T. Wu, A. Yahia-Ammar, F. Vetrone and N. Hildebrandt, *Eur. J. Inorg. Chem.*, 2017, **2017**, 5186–5195.
43 V. I. Sokolov, A. V. Zvyagin, S. M. Igumnov, S. I. Molchanova, M. M. Nazarov, A. V. Nechaev, A. G. Savelyev, A. A. Tyutyunov, E. V. Khaydukov and V. Y. Panchenko, *Opt. Spectrosc.*, 2015, **118**, 609–613.
44 R. B. Anderson, S. J. Smith, P. S. May and M. T. Berry, *J. Phys. Chem. Lett.*, 2014, **5**, 36–42.
45 N. U. Wetter, A. M. Deana, I. M. Ranieri, L. Gomes and S. L. Baldochi, *IEEE J. Quantum Electron.*, 2010, **46**, 99–104.
46 S. Fischer, H. Steinkemper, P. Löper, M. Hermle and J. C. Goldschmidt, *J. Appl. Phys.*, 2012, **111**, 013109.
47 M. Kaiser, C. Würth, M. Kraft, T. Soukka and U. Resch-Genger, *Nano Res.*, 2019, **12**, 1871–1879.
48 J. Dormand and P. Prince, *J. Comput. Appl. Math.*, 1980, **6**, 19–26.